Defense Threat Reduction Agency
8725 John J. Kingman Road, MS
6201 Fort Belvoir, VA 22060-6201

DTRA-TR-21-35

TECHNICAL REPORT

Radiation Effects in Ultra-Wide Bandgap AlN and Diamond Schottky Diodes

May 2021

HDTRA1-17-1-0041

Prepared by: Yuji Zhao

Arizona State Univeristy
Tempe, AZ 85281

REPORT DOCUMENTATION PAGE

Form Approved
OMB No. 0704-0188

1. REPORT DATE *(DD-MM-YYYY)*	2. REPORT TYPE	3. DATES COVERED *(From - To)*
04-08-2021	Final Report	5/3/2017 - 11/2/2020

4. TITLE AND SUBTITLE
Radiation Effects in Ultra-Wide Bandgap AlN and Diamond Schottky Diodes

5a. CONTRACT NUMBER

5b. GRANT NUMBER
HDTRA1-17-1-0041

5c. PROGRAM ELEMENT NUMBER
N/A

6. AUTHOR(S)
Yuji Zhao

5d. PROJECT NUMBER

5e. TASK NUMBER

5f. WORK UNIT NUMBER

7. PERFORMING ORGANIZATION NAME(S) AND ADDRESS(ES)
Yuji Zhao, Arizona State University

8. PERFORMING ORGANIZATION REPORT NUMBER

9. SPONSORING/MONITORING AGENCY NAME(S) AND ADDRESS(ES)
Defense Threat Reduction Agency
8725 John J. Kingman Road
Fort Belvoir, VA 22060-6201

10. SPONSOR/MONITOR'S ACRONYM(S)
DTRA

11. SPONSOR/MONITOR'S REPORT NUMBER(S)
N/A

12. DISTRIBUTION/AVAILABILITY STATEMENT
Approved for public release; Distribution is unlimited

13. SUPPLEMENTARY NOTES
None

14. ABSTRACT
We performed comprehensive studies on the radiation effects on UWBG AlN and Ga2O3 materials. Proton, electron, and gamma-ray irradiation experiments were performed on UWBG semiconductors as well as on Schottky diodes. Material and device characterizations such as I-V, C-V, XRD, AFM and DLTS were conducted to investigate the radiation damage processes. Key information in defect levels, dose effects on electrical performance and crystal qualities, were obtained. The results were published in peer-reviewed journals and international conferences. This work will significantly advance fundamental knowledge in radiation effects in emerging UWBG devices, critical to various DoD applications.

15. SUBJECT TERMS
Wltra wide bandgap semiconductors, radiaton effects, electronics

16. SECURITY CLASSIFICATION OF:			17. LIMITATION OF ABSTRACT	18. NUMBER OF PAGES	19a. NAME OF RESPONSIBLE PERSON
a. REPORT	b. ABSTRACT	c. THIS PAGE			Yuji Zhao
U	U	U	UU	16	19b. TELEPHONE NUMBER *(Include area code)* 480-727-4450

DTRA Basic Research Final Report

Project Title: Radiation Effects in Ultra-Wide Bandgap AlN and Diamond Schottky Diodes

Grant/Award #: HDTRA11710041
PI Name: Yuji Zhao
Organization/Institution: Arizona State University

1. Project Goals, Team and Facilities

1.1. Project goals

The objective of this DTRA YIP research plan is to elucidate and advance our knowledge of the fundamental physics of radiation effects on ultra wide bandgap (UWBG) semiconductors and devices, such as AlN, diamond and Ga_2O_3. Proton, electron, and gamma-ray irradiation experiments will be performed on UWBG semiconductors as well as on Schottky diodes. Comprehensive material and device characterizations will be conducted to investigate both ionization and displacement damage processes. Key topics in radiation effects such as total dose effects, energy levels of radiation defects, carrier removal rates, role of pre-existing defects, and thermal stabilities of radiation defects will be studied, and their impacts on the devices discussed. Experimental observations will be validated through theoretical modeling to explore the physical mechanisms behind the radiation effects. This work will significantly advance fundamental knowledge in radiation effects in emerging UWBG devices, and provide basic guidance for the design and fabrication of next-generation radiation-insensitive UWBG RF and power devices, critical to various DoD applications.

1.2. Project team

The key personnel from Arizona State University (ASU) have extensive experience and proven expertise in characterizing and modeling radiation effects in semiconductor materials, devices, and ICs, reliability and radiation effects testing, and nano-scale material characterization. The principal investigator Dr. Yuji Zhao is an Associate Professor at ASU, and a recognized expert in materials science and device engineering of UWBG materials and devices including AlN, Ga_2O_3, and diamond. He has a strong track of record in UWBG research with over 180 journal papers and conference proceedings and over 20 patents. The research team also include Ph.D. students in Dr. Zhao's group who carried out the theoretical and experimental work under Zhao's guidance.

1.3. Facilities

The research work is performed in Tempe/Phoenix, Arizona, where ASU is located. The material characterization, device fabrication, electrical testing, and radiation studies are conducted at ASU facilities which include a state-of-the-art nanofabrication facility (ASU NanoFab), materials characterization facility (ASU Eyring Materials Center), radiation sources (ASU Co-60 gamma radiation chamber, ASU iBeAM MeV ion beam source), and high-performance computing facilities (ASU Research Computing Center). Some additional irradiation activities for this program are occasionally performed at Sandia National Laboratories in Albuquerque, NM.

2. Radiation Effects in UWBG AlN Materials and Devices

2.1. Overview

The radiation hardness of a semiconductor is a critical material quality for the design and fabrication of radiation-insensitive semiconductor electronic devices and systems for various extreme environments such as space missions, advanced military operations, and nuclear power stations. Recently, the UWBG semiconductor AlN, which has a bandgap (E_g ~ 6.2 eV) significantly larger than GaN (E_g ~ 3.4 eV), has emerged as an attractive material candidate for next-generation radiation-insensitive power and RF electronic applications. Their advantageous material properties include a WBG of 6.2 eV, a tough chemical bonding rated at 11.52 eV/atom, a high-electron mobility of 1090 $cm^2/V{\cdot}s$, a high-critical field (E_c) of 12 mV/cm, and a high maximum operating temperature of 690°C. Since the radiation tolerance nonlinearly scales with the bandgaps of the materials, superior radiation hardness can also be expected from UWBG AlN. Despite the high-potential AlN, there are currently a very few reports in the literature that discuss the radiation effects in AlN materials and devices mainly due to the challenges in producing high-quality AlN crystals and reliable AlN devices.

We performed basic characterizations on the radiation effects in AlN Schottky diodes under gamma-ray and proton irradiation, which includes basic device characterizations such as current-voltage (I-V), capacitance-voltage (C-V), and high-temperature measurement; as well as material characterizations such as x-ray diffraction (XRD), atomic force microscope (AFM), and scanning electron microscope (SEM) measurement. These results will help us to obtain a basic understanding on the radiation effects in AlN Schottky diodes.

2.2. Device structures

MOCVD was used to grow AlN epilayers on a single-side polished (0001) sapphire substrate. The epilayers consisted of an AlN buffer layer followed by a 1 µm-thick unintentionally doped (UID) AlN resistive layer and a 300 nm n-AlN layer. A 2 nm GaN capping layer was employed on top of the n-AlN layer to prevent oxidation of the surface. Standard photolithography was used to pattern and expose the contacts. The ohmic contact stack consisted of Ti/Al/Ti/Au (20 nm / 100 nm / 20 nm / 50 nm). The Schottky contact stack consisted of Pt/Au (30 nm / 120 nm). The devices consisted of circular ohmic and Schottky contacts, which were 400 µm and 200 µm in diameter, respectively. The lateral separation distance between the two contacts is 200 µm. Additionally, we fabricated double-circle AlN Schottky diodes, where the diameter of the ohmic and Schottky contacts is 260 µm and 100 µm, respectively. The details of the AlN device structure are shown in Fig. 1.

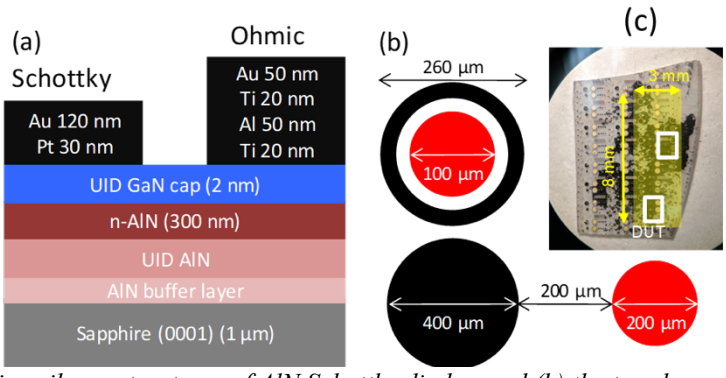

Fig. 1. (a) The schematic epilayer structures of AlN Schottky diodes, and (b) the top-down views of the double-circle and lateral AlN Schottky diodes, and (c) the image of the fabricated AlN sample.

2.2. Proton irradiation

AlN Schottky diodes were subjected to proton irradiation using 3 MeV protons at four different fluxes: 5×10^{9} cm^{-2}, 5×10^{11} cm^{-2}, 5×10^{13} cm^{-2}, and 5×10^{15} cm^{-2}. Electrical and material characterization analysis was performed before and after each radiation dose to quantify the change in device characteristics. It was found that the AlN Schottky diodes performed reliably up to a proton irradiation dose of 5×10^{13} cm^{-2}, with little or no change in the key device performance such as current, turn-on voltage, ideality factor, and breakdown voltage, etc. The performance of the AlN devices showed a significant degradation after a high dose irritation of 5×10^{15} cm^{-2}, where the current of the devices dropped two orders of magnitude. Material and surface characterizations via AFM, XRD, and SEM indicated a consistent degradation in the AlN bulk crystal quality and a drastic increase in surface roughness.

Figure 2 shows the forward-bias I-V characteristics of the AlN Schottky diodes under different proton irradiation dose. The devices perform consistently and reliably up to the dose of 5×10^{13} cm^{-2}. After the highest proton dose of 5×10^{15} cm^{-2}, the current of the devices drop by two orders of magnitude.

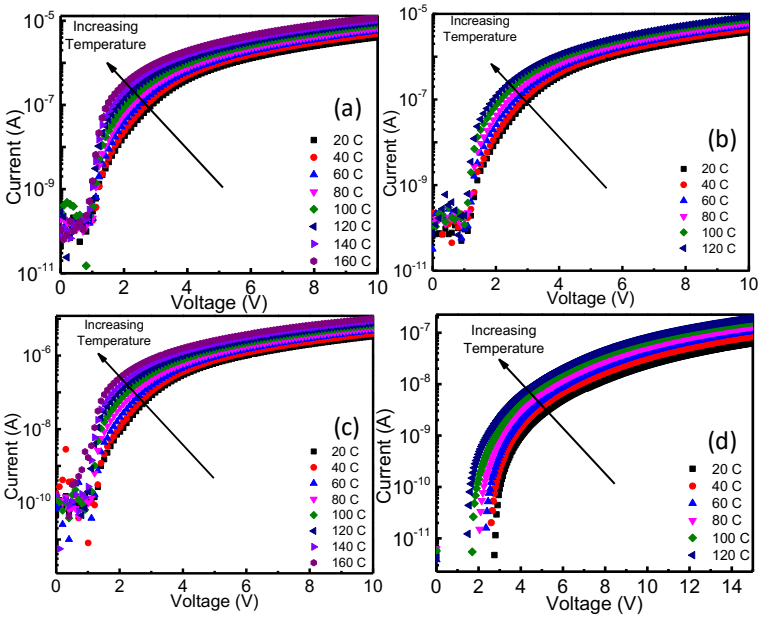

Fig. 2. Forward-bias I-V characteristics from 20 to 120°C for AlN Schottky diodes under various proton irradiation doses: (a) No radiation, (b) 5×10^{9} cm^{-2}, (c) 5×10^{13} cm^{-2}, and (d) 5×10^{15} cm^{-2}.

Figure 3 shows the reverse-bias I-V characteristics of the AlN Schottky diodes under various proton irradiation dose. As predicted by the thermionic emission model, the current magnitudes of the AlN devices increase with the increasing temperatures. Up to the dose of 5×10^{13} cm^{-2}, the current magnitudes of the devices are difficult to distinguish from one another, indicating that the AlN Schottky diodes are resisting radiation-induced degradation at least up to this flux. At the dose of 5×10^{15} cm^{-2}, the reversed I-V characteristics of the devices showed a significant degradation, which is consistent with the forward I-V results.

Figure 4 shows the C-V characteristics of the AlN Schottky diodes under various proton irradiation dose. The C-V characteristics remain relatively unchanged up to the proton dose of 5×10^{13} cm^{-2}. After the dose of 5×10^{15} cm^{-2}, the C-V curves of the AlN devices collapsed. The

effective carrier concentration in the n-AlN layer could be extracted from the C-V results, which is around 10^{14} cm^{-3} and does not deviate up to the proton dose of 5×10^{13} cm^{-2}. After the dose of 5×10^{15} cm^{-2}, the effective carrier concentration cannot be reliably approximated.

XRD scans were used to determine the crystal quality change as a function of radiation dose. The full-width-at-half-maxima (FWHM) values, presented in Fig. 5, can be seen rising after each radiation dose. This indicates a degradation in the crystal bulk. The sharp increase after the 10^{11} cm^{-2} dose followed by a decrease can be attributed to small differences in the experimental setup.

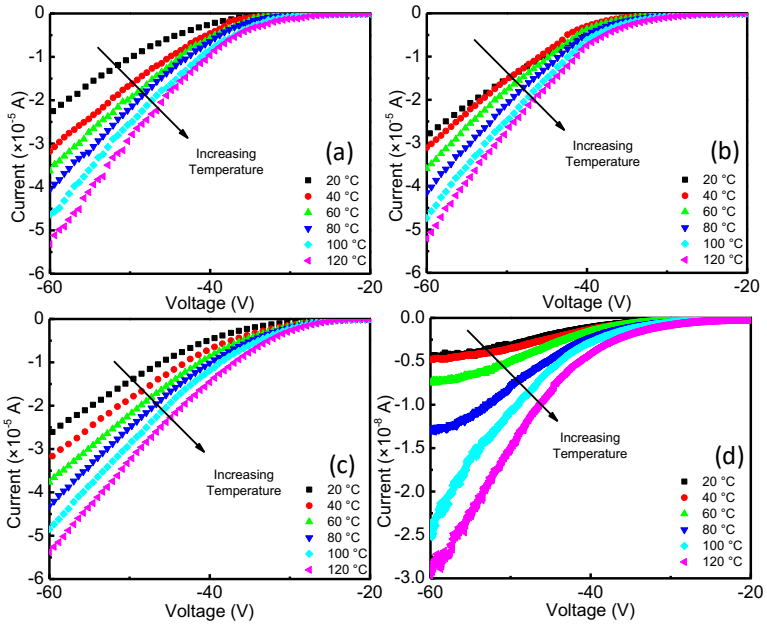

Fig. 3. Reverse-bias I-V characteristics from 20 to 120°C for AlN Schottky diodes under various proton irradiation doses: (a) No radiation, (b) 5×10^{9} cm^{-2}, (c) 5×10^{13} cm^{-2}, and (d) 5×10^{15} cm^{-2}.

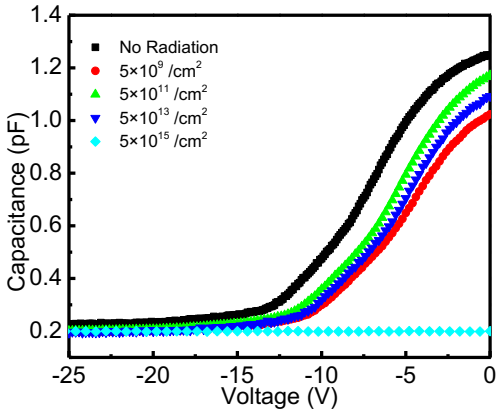

Fig. 4. C-V characteristics for AlN Schottky diodes under various proton irradiation doses.

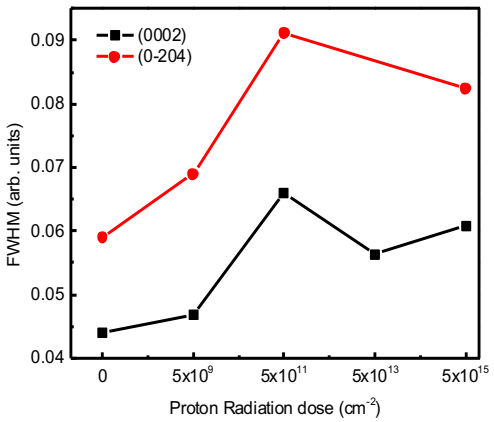

Fig. 5. XRD FWHM values for the AlN materials as functions of proton radiation dose.

AFM scans were carried out to characterize the surface topography of the bombarded regions in AlN Schottky diodes. Figure 6 shows AFM scans after the highest dose in two distinct regions: (1) in a region far away from the irradiated AlN Schottky diodes and (2) in a region directly under the full intensity of irradiation. It was found that region (1) had an average surface roughness of 7.68 nm and region (2) had 16.03 nm. Clearly visible in Region (2) are a number of particulates/surface abnormalities that AFM scans reveal to be between 50 and 150 nm in height on average. These surface features are a ubiquitous find in the irradiated region, but far less so in the un-irradiated region (Region (1)). Furthermore, where they do occur in Region (1), their height is typically much lower, rarely venturing toward 50 nm. A 3-D AFM scan of Region (2) is shown in Fig. 6(b).

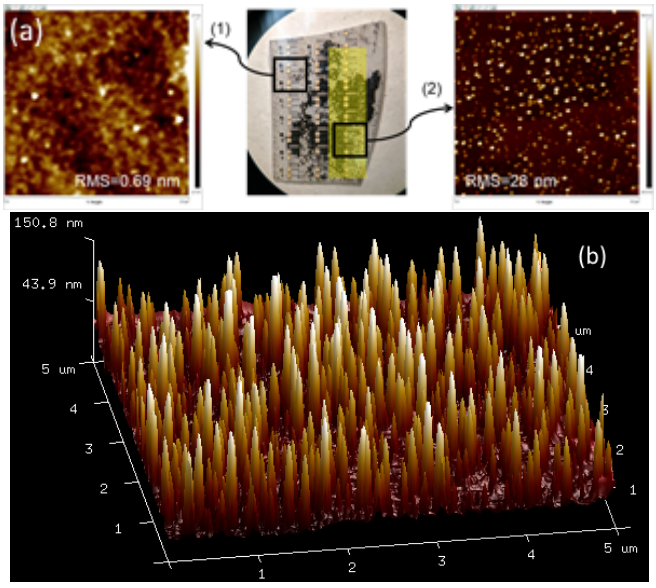

Fig. 6. (a) AFM images in two distinct regions: (1) is a region far away from the proton bombardment, while (2) is directly under the full intensity of the beam. (b) 3D AFM image in Region (2) showing the height of the surface features.

2.2. Electron irradiation

The ohmic contact stack consisted of Ti/Al/Ti/Au (20 nm / 130 nm / 20 nm / 50 nm) were fabricated on 0.1 μm-thick n-doped AlN layer ([Si]=5×10^{17} cm^{-3}). These contacts were tested via

the Transmission Line Model (TLM) method, the details of which can be seen in Fig. 7(a). The experimental results in Fig. 7(b), show decent ohmic behavior. Approximately 80% of the fabricated AlN sample exhibits this ohmic behavior, which is a significant improvement over previously fabricated AlN diodes.

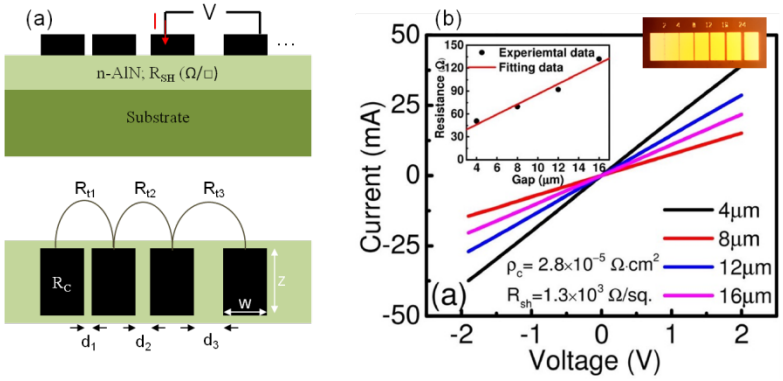

Fig. 7. TLM model and results. (a) Schematic of the AlN TLM pattern. (b) TLM results.

The AlN sample was subjected to 200 keV electron radiation for 1 hour, to achieve a fluence of 10^{18} cm^{-2} inside a Titan Transmission Electron Microscope. After a round of electrical and material characterizations, the sample was re-inserted into the TEM for an additional 2 hours. The results after the electron radiation can be seen in Fig. 8(b). The currents have increased noticeably. This is possibly due to the creation of additional surface states on AlN by the electron radiation.

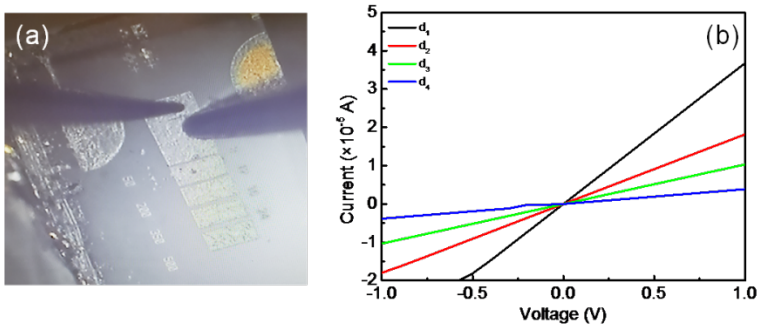

Fig. 8. AlN sample post-irradiation. (a) Optical microscope image of the AlN sample. (b) TLM results.

Material characterization tests were carried out using Atomic Force Microscopy (AFM) scans and High Resolution X-Ray Diffraction (HR-XRD). The AFM scans (Fig. 9) show highly smooth surfaces of the AlN samples prior to irradiation, with a surface roughness root mean square (RMS) of 0.12 nm. After 3 hours of electron radiation, the surface roughness has increased considerably, up to an RMS value of 1.75 nm (Fig. 9(c)). The scan size for each AFM scan is 5×5 μm^2, which is more than adequate for surveying surface roughness. Figures 9(a) and 9(b) show a close-up of the same spot with a scan size of 1×1 μm^2.

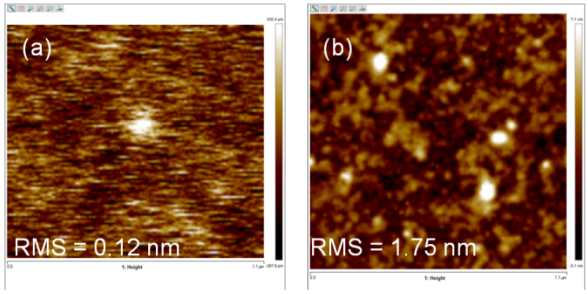

(c)

Radiation Condition	Roughness RMS
Initial	0.12 nm
After 1 Hr	0.12 nm
After 3 Hr	1.75 nm

Fig. 9. AFM scan results. (a) Close-up of the AlN sample as-received. (b) Close-up of the same spot as in (a) after 3 hours of electron radiation. (c) Table summarizing the results of the AFM scans.

HR-XRD scans of the main (002) crystal plane and the secondary (201) crystal plane were carried out using Cu Kα1 radiation (wavelength λ=1.541 Å), and the results are shown in Fig. 10. HR-XRD scans allow one to quantify the crystal quality of a material by analyzing the FWHM values. The lower the FWHM value, the better. The results in Fig. 10 show that while the main (002) plane resists degradation, the crystal quality of (102) plane worsens after 3 hours of electron radiation. Since the (102) plane hosts edge dislocations, it is possible that the electron radiation is creating more edge dislocations.

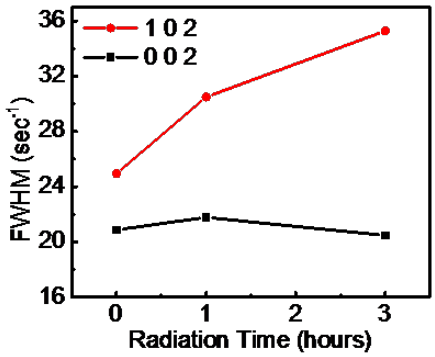

Fig. 10. HR-XRD results of AlN devices with electron radiation.

2.2. Gamma-ray irradiation

AlN Schottky diodes were subjected to gamma-ray irradiation of 30 MRad and 90MRad. Figure 11 shows (a) forward current density vs. voltage characteristics and (b) XRD scan results on AlN Schottky diodes under no radiation, 30 MRad, and 90 MRad gamma-ray irradiation. The results show that the turn-on voltage of the AlN device decreases from 2.2 V under no irradiation to 1.8 V after 90 Mrad irradiation. The forward current density of the devices decreases with each radiation dose. Despite these changes in device characteristics, the XRD scans shows very minimum changes in the crystal qualities of the AlN materials. Figure 11(b) shows that the XRD peaks decreases from 18.08 under no irradiation to 18.02 after 90 MRad, with no changes in the FWHM of the XRD rocking curves. This XRD results indicate that there is almost no degradation in the crystal quality of the AlN materials after a gamma-ray irradiation of 90 MRad, which shows the high radiation tolerance of AlN devices. From the XRD results, we suspect that the changes in the device characteristics of AlN Schottky diodes under gamma-ray irradiation is likely not related to the crystal quality, but due to the changes in surface properties (since the AlN material has a large amount of polarization-induced surface charges).

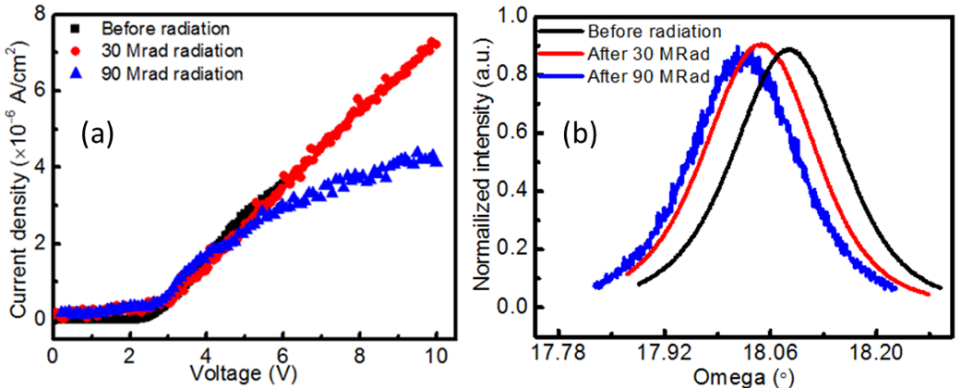

Fig. 11. (a) Forward current density vs. voltage characteristics and (b) XRD scan results on AlN Schottky diodes under no radiation, 30 MRad, and 90 MRad gamma-ray irradiation.

3. Radiation Effects in UWBG Ga_2O_3 Materials and Devices

3.1. Overview

Beta-phase gallium oxide (β-Ga_2O_3) has enjoyed a resurgence in research interest over the past several years. This interest stems from a number of its material properties: the UWBG of 4.6–4.9 eV; a widely tunable n-type conductivity range between 10^{16} and 10^{19} cm^{-3}; a high theoretical breakdown field of 8 MV/cm; a high electron saturation velocity of 2×10^7 cm/s; a large Baliga's Figure of Merit (BFOM) of 3444; and the availability of large high-quality single-crystal substrates. In particular, the UWBG enables deep ultraviolet (DUV), high-power applications, and harsh-environment applications, i.e., operating under ionizing radiation. However, due to their relatively immature statues, very little is known to date on the radiation properties of Ga_2O_3 materials.

We performed basic characterizations on the radiation effects in Ga_2O_3 Schottky diodes under proton irradiation, which includes basic device characterizations such as I-V, C-V, and high-temperature measurement; as well as material characterizations such as XRD, AFM, and DLTS measurements. These results will help us to obtain a basic understanding on the radiation effects in Ga_2O_3 Schottky diodes.

3.2. Device structures

Two types of β-Ga_2O_3 were obtained from Tamura Corporation. The first was an unintentionally doped (UID) ($N_D - N_A \approx 1–4 \times 10^{16}$ cm^{-3}) epi-wafer grown by hydride vapor-phase epitaxy (HVPE) on a Sn-doped ($N_D - N_A \approx 1–20 \times 10^{18}$ cm^{-3}) substrate. The thickness of the UID epilayer is 10 µm, and the thickness of the substrate is 640 µm ± 20 µm. The second substrate was a Sn-doped ($N_D - N_A = 5.5 \times 10^{18}$ cm^{-3}) ($\bar{2}01$) single-crystal substrate grown by the edge-defined film-fed growth (EFG) method. Both substrates were cleaved into small 1 × 1.5 cm^2 samples. For the device fabrication, a large-area backside ohmic contact of Ti/Al/Ti/Au (20 nm / 130 nm / 20 nm / 50 nm) was deposited using e-beam evaporation. This metal layer was subsequently annealed in N_2 ambient at 470°C for 1 min. Standard photolithography was used to pattern and expose several Schottky contacts. There were 100-, 200-, and 300-μm diameter circular Schottky contacts, as well as a square Schottky contact of side length 100 µm. All Schottky contacts consisted of Ni/Au (30 nm / 200 nm) metal stacks. A schematic diagram of the mask used to pattern the Schottky contacts, as well as an optical image of a finished sample, is shown in Fig. 12.

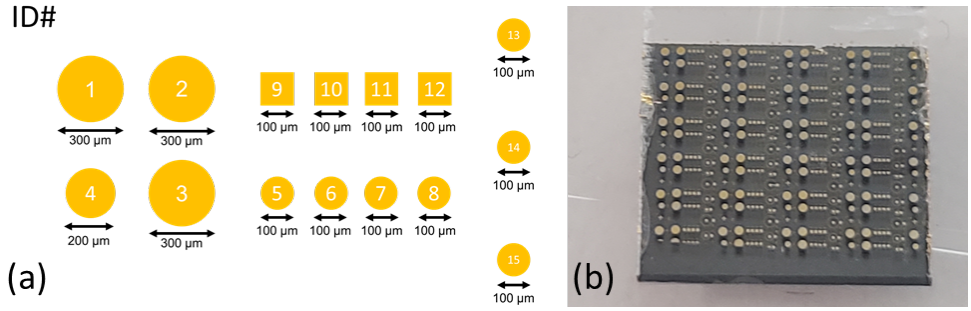

Fig. 12. Photolithography mask used to pattern Schottky contacts and a finished sample. (a) Photo mask with each contact labelled. The ID# in the top left identifies a single block of devices. Each block, which measures approx. 3×1 mm², contains 15 devices and a fully patterned sample can host a few dozen blocks. (b) Image of a fully patterned sample of β-Ga_2O_3. This 1×1 cm² piece hosts a large-area backside ohmic contact (the gray background) and just under 24 blocks of devices (6 rows, 4 columns).

3.3. DLTS analysis (non-irradiated sample)

The DLTS spectra for the $(\bar{2}01)$ sample, split into two temperature regions, are shown in Fig. 13. At temperatures below 200 K, there are broad, smooth extrema visible, which likely correspond to interface states between the semiconductor and the metal. While bulk defects occupy a single discrete energy level in the bandgap, interface states occupy a continuum of energy levels, though emission from energies interface traps in the upper portion of the bandgap will dominate. In Fig. 13(b), we observe a majority carrier (electron) defect between 225 and 250 K with energy 0.46 eV below the conduction band. Based on the changing amplitudes of the DLTS signal, a varying trap concentration can be deduced. Such a situation may arise in the β-Ga_2O_3 samples under study due to the prevalence of surface states. The maximum trap density, N_T, for this defect in the $(\bar{2}01)$ sample was 9.08×10^{15} cm^{-3} over the temperature range where peaks occurred. The lambda effect correction was applied to N_T. As the frequency is increased, the defect can be seen activating at progressively higher temperatures.

The defect often referred to as *E2* in β-Ga_2O_3 (typically 0.78 eV below CBM, and thought to correspond to a Ga vacancy) typically exhibits a peak emission response at T ~ 360 K. This temperature is outside the maximum range for our DLTS cryostat; however, in the $(\bar{2}01)$ β-Ga_2O_3 sample, we observe the "tail" of a majority carrier peak with high DLS signal intensity almost certainly corresponding to *E2*. We are unable to further characterize this defect, but a closer examination of this is shown in Fig. 14.

Upon examining the defect labeled in Fig. 13(b) and considering its activation temperature, energy placement, capture cross section, and trap density, one could reasonably conclude that this defect is likely the *E1* defect. Prior to this study, *E1* has only been observed in epitaxially grown β-Ga_2O_3 materials. We observe the *E1* defect lying at E_C−0.46eV in the $(\bar{2}01)$ bulk sample, occurring at approx. the same temperature region (230–250K) as the aforementioned studies. The lack of response to irradiation and the general omnipresence of *E1* in many studies and growth methods would indicate that the defect is related to impurities. Remarkably, Ingebrigtsen *et al.* demonstrated that bulk and epitaxial wafers [EFG (010), molecular beam epitaxy (MBE) (010), and HVPE (001)] manifest the *E1* defect at nearly the exact same energy (E_C−0.56eV) and capture cross section ($0.3 – 5 \times 10^{-13}$cm^2) across several studies. Others have found comparable energies for *E1*, though trap densities and capture cross sections vary up to two orders of magnitude. These inconsistencies may be a consequence of different test settings and device fabrication. Materials grown by bulk growth methods such as Czochralski and EFG typically exhibit higher trap densities

for *E1* and other defects. It has been suggested that the electron trap *E1* may be due to Fe or Co impurities, possibly incorporated during the growth process.

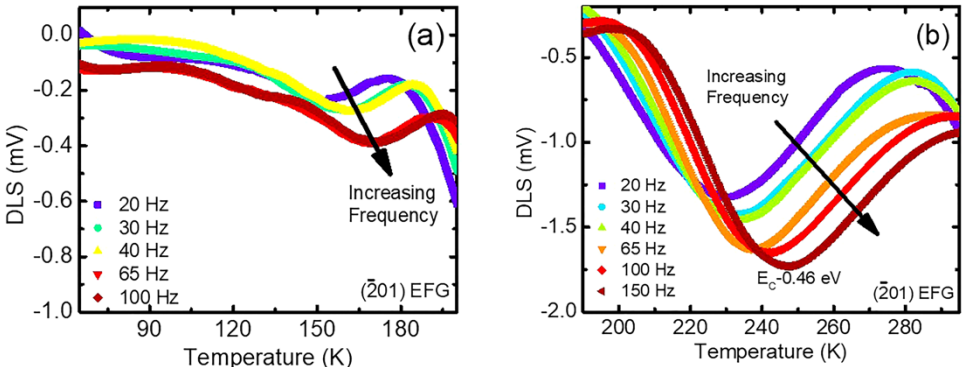

Fig. 13. DLTS data obtained from $(\bar{2}01)$ *β-Ga_2O_3 crystals grown by EFG. Measurements performed with: quiescent reverse bias $V_R = -0.4$ V; pulse voltage $V_1 = 0.1$ V; pulse width = 20 µs; temperature ramp rate = −100 mK/s. (a) DLTS data from 75 to 200 K. (b) DLTS data from 180 to 300 K. Note the vertical scale difference of the two regions.*

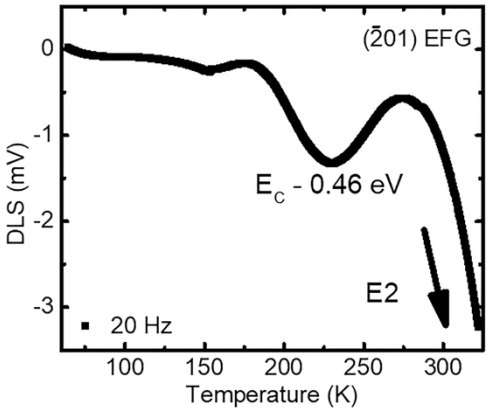

Fig. 14. DLTS data obtained from $(\bar{2}01)$ *β-Ga_2O_3 crystals grown by EFG. Measurement performed with: quiescent reverse bias $V_R = -0.4$ V; pulse voltage $V_1 = 0.1$ V; pulse width = 20 µs; temperature ramp rate = −100 mK/s. This scan was taken out to a higher temperature, showing the low-temperature side of the prominent E2 defect present in all β-Ga_2O3 materials.*

For the (001) HVPE sample, there is excellent agreement in activation temperatures (325K) and reasonable overlap in the bandgap position between this study and the *E2** defect cited by others. Furthermore, the defect *E2** has a rather characteristic placement in the spectrum, riding the low-temperature shoulder of the prominent *E2* defect. These remarkable similarities would lead one to suspect that the defect in Figs. 15(a) and 16 is *E2*;* however, *E2** has hitherto been detected only after low-energy (600 keV ... 1 MeV) proton irradiation was applied. Polyakov *et al.* did not observe the defect at all after high energy (10 MeV) proton irradiation was applied. These inconsistencies may be due to any number of differences in testing setups and sample preparation. Regardless, the E_C−0.46 eV defect visible in Fig. 15(a) seems to be a prime candidate for *E2** designation in spite of no proton irradiation occurring in this study. The exact origin of *E2** has been suggested to be V_{Ga} or complexes thereof, as its signature has appeared in bulk EFG (010) and epitaxial HVPE (001), MBE (010) samples post-irradiation. This study revealed what is likely the *E2** defect in the absence of any radiation treatments. It is possible that the annealing step in the fabrication of our Schottky diodes may have been the thermal treatment catalyst for a weak

*E2** signal to appear. Whatever the case, *E2** is regarded as an intrinsic defect or a complex involving intrinsic elements. The electron trap *E2* (different from *E2**) is a ubiquitous finding in essentially every DLTS study performed to date on β-Ga_2O_3, though it was not considered in this study. Several recent studies employing secondary ion mass spectrometry (SIMS) have assigned *E2* to be from a Fe_{Ga} substitution, with some preference to the octahedral Ga sites. Bulk growth methods, such as Czochralski and EFG (this study), often require the use of an Ir crucible, where contamination from Ir and residual Fe is likely. Epitaxial growth methods, e.g., MBE and HVPE (this study), do not require an Ir crucible and will naturally have less Fe contamination, again consistent with this study.

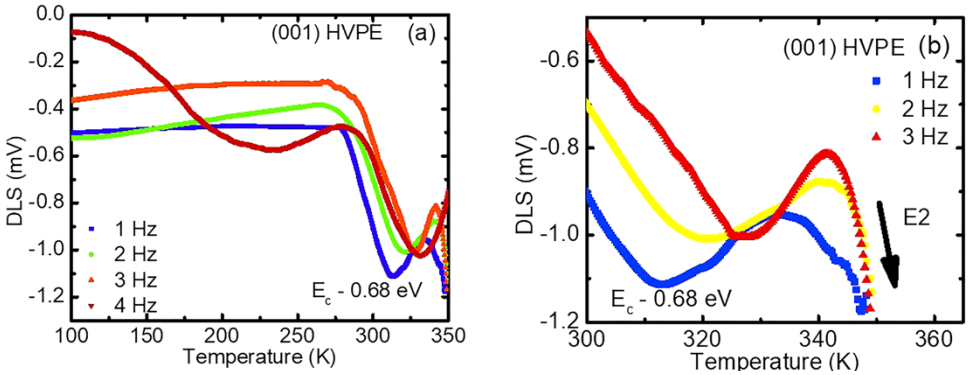

Fig. 15. DLTS data obtained from (001) β-Ga_2O_3 epilayers grown by HVPE. Measurement settings are quiescent reverse bias $V_R = -6$ V; pulse voltage $V_1 = 1$ V; pulse width = 10 ms; temperature ramp rate = −100 mK/s. (a) DLTS data for the 100–350 K temperature region. The 4 Hz scan shows the distinct smooth modulation typical of interface while the others do not, which we attribute to detection thresholds. (b) The 300–350 K temperature region magnified, showing the front "tail" end of the E2 defect.

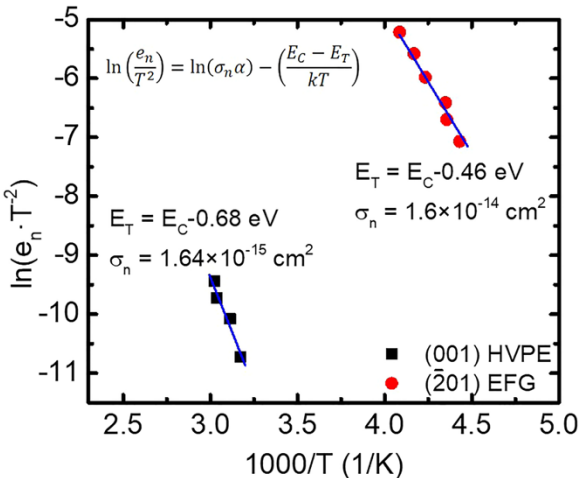

Fig. 16. Arrhenius plot for the EFG-grown and HVPE-grown (001) samples. The electron effective mass used is 0.28m.

3.4. Proton irradiation

The Ga_2O_3 Schottky diode devices were irradiated with 1 MeV protons at several fluences (10^9, 10^{11}, and 10^{13} cm^{-2}) at Sandia National Laboratories. The modus operandi for radiation treatment is as follows: prior to irradiating, many blocks on the sample were tested, to ensure reliable diode performance. Then, several distinct, spatially separate blocks were designated as

"radiation zones"; i.e., one block would be irradiated to a fluence of 10^9 cm^{-2}, another at 10^{11} cm^{-2}, and another at 10^{13} cm^{-2}. For redundancy, in a few cases multiple blocks were used as identical radiation zones. The incident proton spot size used at Sandia was adjusted to cover an entire block while shielding the rest of the sample from irradiation. Any blocks not irradiated can be treated as initial condition devices for comparison. The electrical (I-V and C-V) characteristics of the β-Ga_2O_3 devices was tested using a Keithley 4200 Semiconductor Characterization System (SCS) and Keithley 2657A High Power System Source Meter. The forward bias data for a representative contact of each geometry are shown in Fig. 17. The current collapses after the highest radiation dose of 10^{13} cm^{-2}, indicating significant damages to the devices.

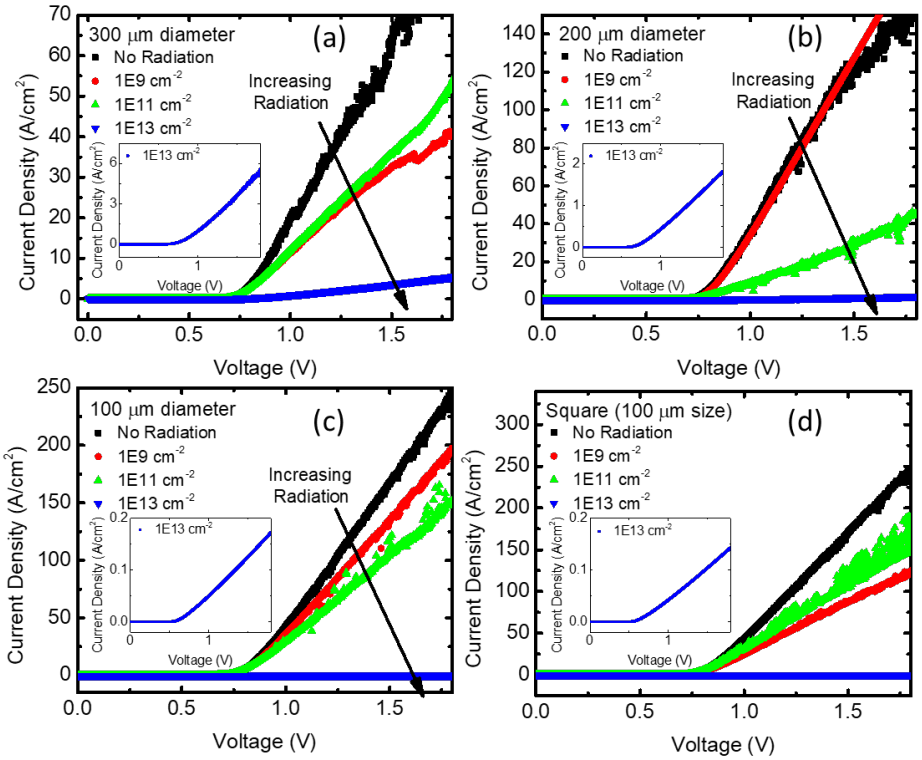

Fig. 17. Forward bias I-V data for the irradiated 001 Ni/Au Ga_2O_3 Schottky diodes as a function of radiation fluence, sorted by contact geometry. (a) Forward bias data for the 300 μm-diameter contact. Inset: Forward bias data for the 10^{13} cm^{-2} fluence, magnified. (b) Forward bias data for the 200 μm-diameter contact. Inset: Forward bias data for the 10^{13} cm^{-2} fluence, magnified. (c) Forward bias data for the 100 μm-diameter contact. Inset: Forward bias data for the 10^{13} cm^{-2} fluence, magnified. (d) Forward bias data for the square contact of side 100 μm. Inset: Forward bias data for the 10^{13} cm^{-2} fluence, magnified. The trend of increasing radiation fluence resulting in lower current magnitudes is slightly broken between the 10^{11} and 10^{13} cm^{-2} cases. All data taken at room temperature (~20°C).

Figure 18 shows reverse bias data gathered from an initial test run of the irradiated diodes and Table 1 shows breakdown data. A larger sample size is currently being tested and analyzed. Breakdown is defined here as the voltage at which the current density equals −1 mA/cm^2. Occasionally, a device will experience destructive breakdown (DBD), where the contact becomes destroyed and then untestable. This is usually due to too large a current running through the device
and can usually be mitigated by using smaller voltage increments or terminating the voltage sweep before the threshold at which DBD occurs. If DBD occurs before the breakdown threshold of −1 mA/cm^2 current density is reached, a breakdown voltage cannot be determined. Notably, in the

dataset below, the square contacts experience DBD in nearly all cases. This may be to do with electric field crowding about the sharp corners.

Both Fig. 18 and Table 1 show a clear trend of increasing breakdown voltage with increasing proton fluence, rising sharply from the devices where no radiation was applied compared to devices where the highest fluence (10^{13} cm^{-2}) was applied. This finding is a contrast to previous radiation work done on a similar material, AlN, which also has an ultra wide bandgap (6.2 eV) like β-Ga_2O_3 (4.6–4.9 eV); however, in that study, protons of much higher energy were used (3 MeV). Based on recent simulations done in SRIM, it was deduced that for the β-Ga_2O_3 material, protons of energy 1 MeV would deposit much more energy within the depletion region of the devices than 3 MeV protons. Hence, 1 MeV protons would likely have a more drastic effect on device performance compared to 3 MeV protons.

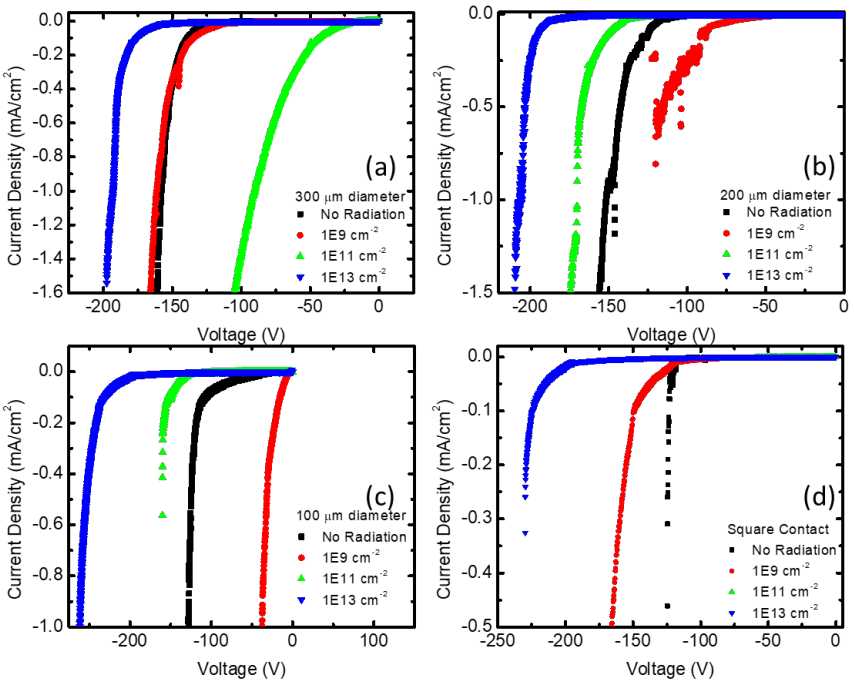

Fig. 18. Reverse bias I-V data for the irradiated 001 Ni/Au Schottky diodes as a function of radiation fluence, sorted by contact geometry. (a) Reverse bias data for the 300 μm-diameter contact as a function of radiation fluence. (b) Reverse bias data for the 200 μm-diameter contact as a function of radiation fluence. (c) Reverse bias data for the 100 μm-diameter contact as a function of radiation fluence. (d) Reverse bias data for the square contact of side 100 μm. The 10^{11} cm^{-2} test experiences extremely premature breakdown.

Fluence [protons/cm^2]	300 um BD [V]	200 um BD [V]	100 um BD [V]	Square BD [V]
No Radiation	157.9	151.8	127.7	>124 (DBD)
10^9	161.2	>120 (DBD)	37.5	172.9
10^{11}	90.3	170.1	>160.1 (DBD)	>59 (DBD)
10^{13}	192.9	206.6	261.7	>229.8 (DBD)

Table 1. Breakdown data for the irradiated 001 Ni/Au Schottky diodes as a function of radiation fluence and contact geometry. Extracted from Fig. 3. DBD = destructive breakdown, this label means that the true breakdown voltage could not be determined due to premature contact destruction. The breakdown voltage will always be higher than the labelled value in these cases. This dataset represents an initial test run.

The capacitance-voltage data is shown in Fig. 19. There is a clear trend in all cases that as fluence increases, the capacitance decreases, possibly due to the recombination of carriers. With increasing size, the capacitance increases, due to the fact that the area of any arbitrary contact is directly proportional to its capacitance. However, it should be noted that, although negligible, the square contact has a slightly larger area than the 100 µm diameter circular contact.

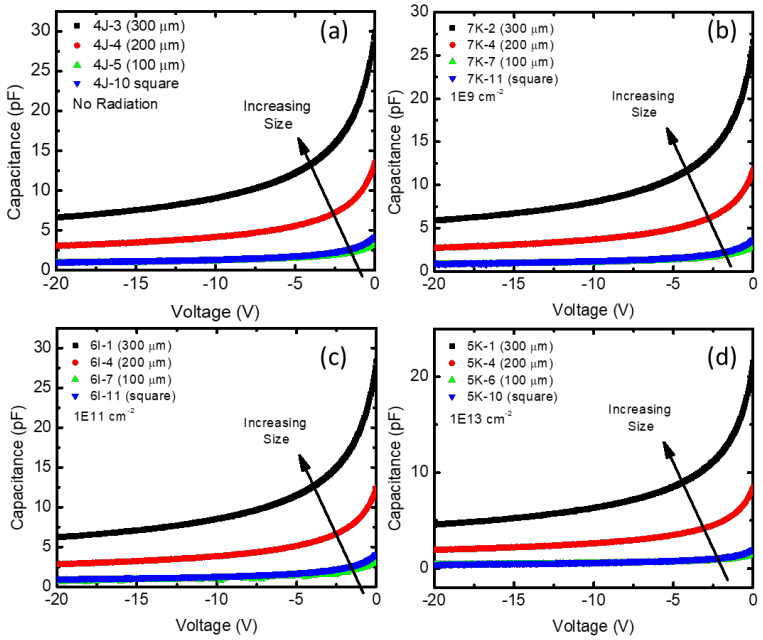

Fig. 19. Capacitance-voltage data for the irradiated 001 Ni/Au Schottky diodes, taken at 300 K. (a) C-V data for the devices not exposed to any radiation. (b) C-V data for the devices exposed to 10^{9} cm^{-2} fluence. (c) C-V data for the devices exposed to 10^{11} cm^{-2} fluence. (d) C-V data for the devices exposed to 10^{13} cm^{-2} fluence. All data gathered at 300 K.

The crystal quality of the sample pre and post radiation is shown in Fig. 20. High resolution x-ray diffraction (HR-XRD) was employed by a PANalytical X'Pert PRO diffractometer, and the rocking curve was analyzed to determine FWHM of each signal. The irradiated curve shows an aggregate measurement of the irradiated sample, as the instrument's spot size for measurement covers the entire sample, and distinct regions cannot be scrutinized. The irradiated curve does show a material decline in crystal quality due to the increased FWHM compared to the pre-radiation case. Protons are much heavier than electrons and gamma rays; it is much more likely that in addition to ionization damage, they will commit atomic displacement damage as well, which would naturally disrupt the crystal structure. The slight shift in position (angle ω) is not a physical result, and is simply due to a small difference in testing conditions, which do not impact the measurement.

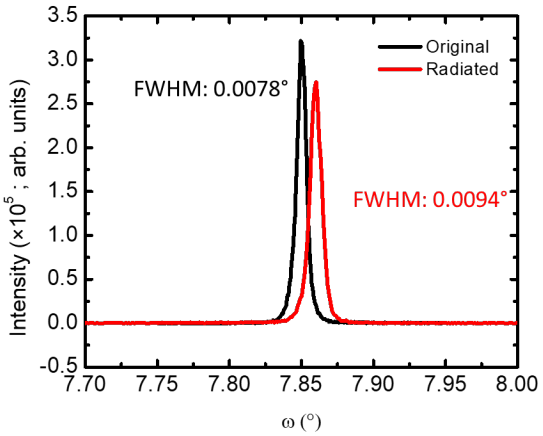

Fig. 20. High-resolution x-ray diffraction (HR XRD) crystal scan for the 001 sample, before and after irradiation. The radiated sample XRD data is an average of the entire sample, which was irradiated in various spots to the three fluences (10^9, 10^{11}, and 10^{13} cm^{-2}).

4. Publications

We have published 2 journal papers and 7 conference presentations from this project. We submitted another 2 papers to IEEE NSREC 2021.

Journal publication

(1) J. Montes, C. Kopas, H. Chen, X. Huang, T. H. Yang, K. Fu, C. Yang, J. Zhou, X. Qi, H. Fu, and Y. Zhao, "Deep level transient spectroscopy investigation of ultra-wide bandgap (-201) and (001) β-Ga_2O_3", *J. Appl. Phys.* **128**, 205701 (2020).

(2) J. Montes, T. H. Yang, H. Fu, H. Chen, X. Huang, K. Fu, I. Baranowski, and Y. Zhao, "Effect of proton radiation on ultra-wide bandgap AlN Schottky barrier diodes", *IEEE Trans. Nucl. Sci.* **66**, 91 (2019).

Conference publication:

(1) J. Montes, C. Kopas, H. Chen, X. Huang, T. H. Yang, K. Fu, C. Yang, J. Zhou, X. Qi, H, Fu, and Y. Zhao, "Deep Level Transient Spectroscopy Investigation of Ultra-Wide Bandgap (-201) and (001) β-Ga_2O_3", *2021 Compound Semiconductor Week (CSW 2021) and the 47th International Symposium on Compound Semiconductors (ISCS 2021)*, May 2021, Stockholm, Sweden, Oral Presentation. (Online).

(2) J. Montes, H. Fu, H. Chen, X. Huang, T. H. Yang, K. Fu, C. Yang, J. Zhou, X. Qi, X. Deng, and Y. Zhao, "Examining deep-level defects in (-201) β-Ga2O3 by deep level transient spectroscopy", *The 62rd Electronic Materials Conference (EMC 2020)*, June 2020, Columbus, OH, Oral Presentation. (Online).

(3) J. Montes, H. Fu, T. H. Yang, H. Chen, X. Huang, K. Fu, I. Baranowski, and Y. Zhao, "Effects of 3 MeV proton radiation on ultrawide bandgap aluminum nitride Schottky barrier diodes", *The 13th International Conference on Nitride Semiconductors 2019 (ICNS-13)*, Jul 2019, Bellevue, WA, Poster Presentation.

(4) Y. Zhao, J. Montes, H. Fu, K. Fu, X. Huang, H. Chen, T. H. Yang, and I. Baranowski, "Progress on radiation effects in ultra-wide bandgap AlN Schottky barrier diodes", *2018 IEEE Nuclear and Space Radiation Effects Conference (IEEE NSREC 2018)*, Jul 2018, Kona, HI, Poster Presentation (Late News).

(5) J. Montes, H. Fu, T. H. Yang, H. Chen, X. Huang, I. Baranowski, K.Fu, and Y. Zhao, "Gamma-ray and proton radiation effects in AlN Schottky barrier diodes", *2018 Compound Semiconductor Week (CSW 2018) and the 45th International Symposium on Compound Semiconductors (ISCS 2018)*, May 2018, Boston, MA, Poster Presentation.
(6) J. Montes, H. Fu, H. Chen, X. Huang, T. H. Yang, I. Baranowski, and Y. Zhao, "Radiation effects in ultra-wide bandgap AlN Schottky barrier diodes", *2018 MRS Spring Meeting*, Apr 2018, Phoenix, AZ, Oral Presentations.
(7) J. Montes, H. Fu, X. Huang, H. Chen, and Y. Zhao, "Radiation effects in ultra-wide bandgap AlN Schottky diodes", *2018 Government Microcircuit Applications and Critical Technology Conference (GOMACTech 2018)*, Miami, FL, Mar 2018, Oral Presentations.

5. Summary

We performed comprehensive studies on the radiation effects on UWBG AlN and Ga_2O_3 materials. Proton, electron, and gamma-ray irradiation experiments were performed on UWBG semiconductors as well as on Schottky diodes. Material and device characterizations such as I-V, C-V, XRD, AFM and DLTS were conducted to investigate the radiation damage processes. Key information in defect levels, dose effects on electrical performance and crystal qualities, were obtained. The results were published in peer-reviewed journals and international conferences. This work will significantly advance fundamental knowledge in radiation effects in emerging UWBG devices, and provide basic guidance for the design and fabrication of next-generation radiation-insensitive UWBG RF and power devices, critical to various DoD applications.